Designing Ordered Organic Small-Molecule Domains for Ultraviolet Detection and Micrometer-Sized Flexible Imaging

Tingting Yan,[∥] Jinfeng Ge,[∥] Li Su, Xinya Liu, and Xiaosheng Fang*

ACCESS | Metrics & More | Article Recommendations | Supporting Information

ABSTRACT: Photodetectors displaying an ultraviolet (UV) spectral response window are typically based on wide-bandgap semiconductors that have long been dominated by inorganic materials that suffer from bottlenecks of low flexibility and a limited material family. Here, we synthesized a novel organic small molecule and controlled its crystallization to suppress leakage currents and facilitate separation of the carriers, and the relationship between the nanoscale phase separation morphology and the optoelectrical performance of the photodetectors is disclosed. Our optimized organic photodetector (OPD) presents a UV spectral response window, with superior self-powered responsivities of 45 mA/W (under 250 nm light) and 70 mA/W (under 300 nm light), outperforming the Si photodiode and rivaling other reported UV self-powered photodetectors. Finally, an imaging system was constructed to demonstrate the application potential of the OPD in UV flexible imaging with high-resolution arrays of 400 pixels × 400 pixels (5 μm × 5 μm per pixel), which could work in bent states and successfully output images of micrometer-sized objects.

KEYWORDS: small-molecule design, crystallization controlling, UV detection, flexible imaging

Photodetectors based on ultraviolet (UV)-sensitive materials can detect UV light and convert it into electric signals that have widespread applications in optical communication, flame detection, and UV imaging.[1−3] Inorganic wide-bandgap semiconductors have occupied the UV detection market for many years but face the bottlenecks of low flexibility and a limited material family.[4] Although a series of low-dimensional wide-bandgap semiconductors have been designed to address this issue, their large-scale growth remains a challenge, limiting their practical application in industry.[5] π-Conjugated organic semiconductors can achieve tunable and strong spectral absorption through molecular structure design, which guarantees the efficient functioning of photodetectors involving exciton generation and separation and transportation of the carriers, which notably enriches the material selection alternatives for next-generation UV-responsive materials. In addition, they can be prepared as high-quality thin films through simple solution methods (spin-coating, spray-coating, and large-area roll-to-roll production) and can be monolithically integrated with silicon readout circuitry.[6,7] Photodetectors based on thin-film organic semiconductors have superior uniformity as well as inherent flexibility, presenting unique advantages in the field of flexible UV imaging.

Compared to organic polymer semiconductors, organic small molecules have intrinsic advantages such as easily tunable molecular design and synthesis, as well as optoelectronic and morphological properties, and exhibit small batch-to-batch synthesis differences due to their definite chemical structure.[8]
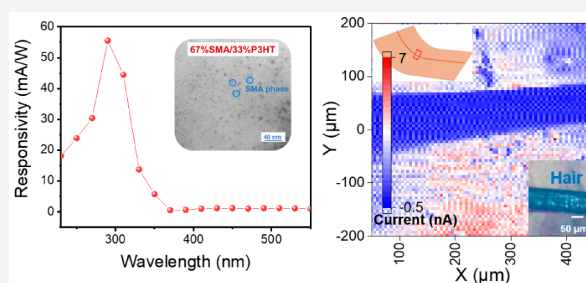
However, to date, UV photodetectors based on thin-film organic semiconductors have rarely been reported. According to traditional views, the thin-film organic semiconductor may not be a preferred choice for UV light detection. Currently, research is mostly focused on narrow-band (∼1.5 eV) organic semiconductors, which may have a photoresponse from 300 to 400 nm,[9] but their peak value of the spectral response window was aroused in the visible to infrared (1−2 μm) regions.[10,11] Meanwhile, the dark state of the photodetector is dominated by the band-to-band thermally generated carriers or band-to-band tunneling,[12] and the dark current will inevitably increase as the bandgap decreases.[13] Thus, photodetectors based on organic semiconductors operating only in the UV spectral response window are scarce.

Here we designed and synthesized a UV-sensitive organic small molecule (SMA) for constructing an organic photodetector (OPD), which presents a spectral response window within the UV region. The crystallization of SMA can be finely regulated by introducing an organic polymer semiconductor: suppressing the large pinholes caused by excessive crystal-
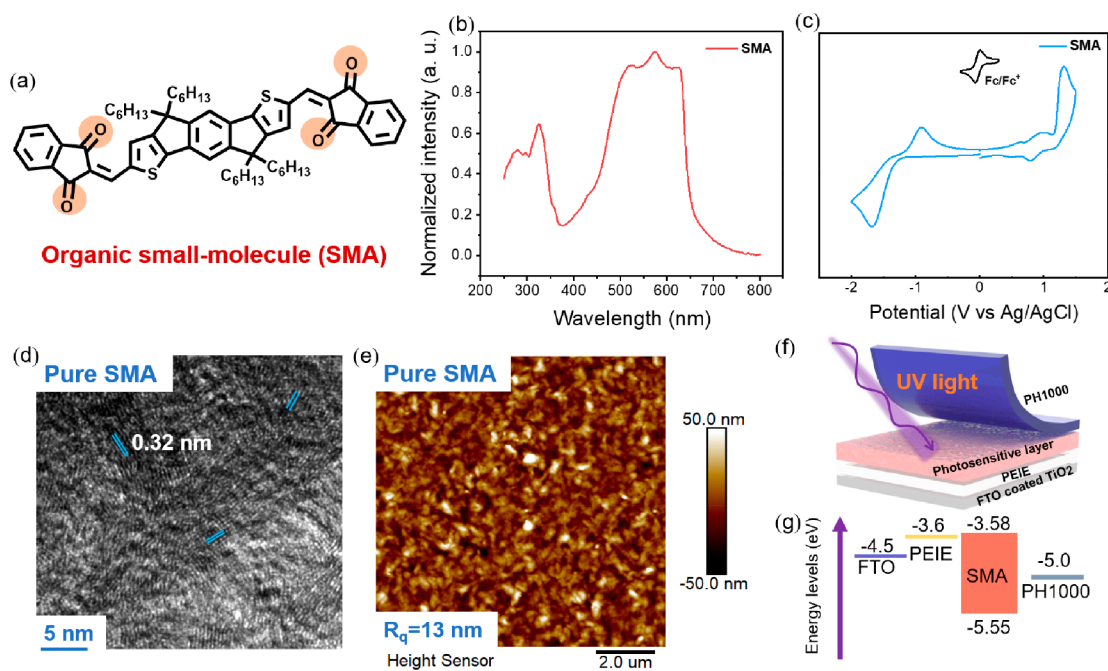
Figure 1. Basic performance of SMA and device configuration of the photodetector. (a) Chemical structure of small molecules (named SMA). (b) Absorption spectrum of SMA. (c) CV curves of SMA (the inset shows the CV curve of ferrocene). (d) High-resolution transmission electron microscopy (TEM) morphology of SMA. (e) Surface morphology of the SMA thin film determined by atomic force microscopy. (f) Device structure of a sandwiched photodetector based on the SMA film. (g) Energy levels of different layers in the SMA-based photodetector.
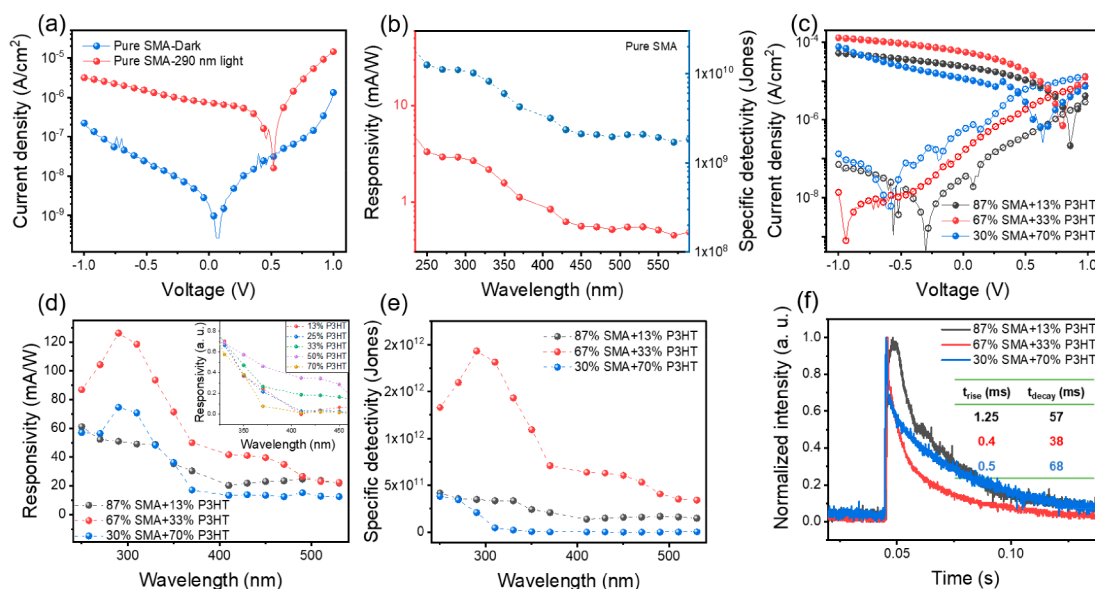
Figure 2. Optoelectronic properties of the photodetector with various P3HT contents doped into SMA. (a) Current density−voltage and (b) responsivity/specific detectivity under different wavelength curves of OPD based on a single SMA component. (c) Current density−voltage, (d) responsivity, and (e) specific detectivity under different wavelengths based on a SMA/P3HT blend with various contentment's P3HT doping (13%, 33%, and 70%). The inset shows the normalized responsivities. (f) Response time of OPD with varied contentment's P3HT doping (13%, 33%, and 70%).

lization in organic small-molecule semiconductors thus reducing the dark current of the device and creating appropriate phase-separated interfaces to obtain sufficient separation of charge carriers thus ultimately attaining the highly sensitive OPD. Surprisingly, a small amount of P3HT (33%) could induce organic small molecule SMA to be uniformly dispersed with suppressed defects, affording a good phase morphology for charge separation. On the basis of this hybrid film (67% SMA/33% P3HT), we demonstrate a self-powered OPD with high responsivities of 45 mA/W (under 250 nm light) and 70 mA/W (under 300 nm light), presenting a better UV response than Si photodiodes. As a demonstration, the OPD was used to realize micrometer-sized flexible UV images, which can accurately output the shape of micrometer-sized objects and work in a bent state to achieve imaging of curved objects.

Small molecule SMA consists of a facile core of indacenodithiophene and planar terminal groups of 1,3-

indanedione, as shown in Figure 1a. The good planarity and structural symmetry of the molecule could provide strong $\pi-\pi$ stacking and crystallinity, which promote exciton extraction and charge transport. More importantly, the four carbonyl groups provide good absorption in the UV region from ~270 to 285 nm, which enables UV detection for photodetectors, as shown in Figure 1b. SMA was synthesized by a one-step simple reaction of Knoevenagel condensation, and the corresponding chemical structure could be identified by NMR and mass spectra, as shown in the Supporting Information. HOMO (highest occupied molecular orbital) and LUMO (lowest unoccupied molecular orbital) energy levels were measured by cyclic voltammetry, as shown in Figure 1c. According to the equation $E_{HOMO/LUMO} = -(\varphi_{ox/red} - \varphi_{Fc/Fc^+} + 4.8)$ eV, the HOMO and LUMO energy levels were calculated as −5.55 and −3.58 eV, respectively, corresponding to a bandgap of 1.97 eV. Tight $\pi-\pi$ stacking was observed from the high-resolution morphology diagram of SMA via transmission electron microscopy (TEM) analysis, with a spacing of ~0.32 nm (Figure 1d), indicating its strong crystallization. In addition, SMA presents a relatively high surface roughness of ~13 nm at the micrometer scale as determined by atomic force microscopy (AFM) analysis, as shown in Figure 1e.

Then we constructed a sandwich-type photodiode to realize the conversion of UV light signals into electric signals of SMA (Figure 1f). Unlike using transparent conductive glass/metal as a pair of electrodes in traditional methods, here we adopted the UV transparent polymer conductor PH1000 electrode as the illumination surface to maximize the probability of UV photons reaching the photosensitive layer,[14] which avoids the UV absorption problem with traditional transparent conductive glass (ITO or FTO) as the illumination surface. A thin PEIE layer was introduced as a charge-blocking layer to increase the barrier and reduce the reverse bias dark current that originated from injection from contacts of the electrode and the photosensitive layer,[15] and the energy levels of each layer are shown in Figure 1g.

The optoelectronic properties of the devices prepared with a pure SMA active layer are shown in panels a and b of Figure 2. This device exhibits photocurrent:darkcurrent ratios of approximately 10−100 when stimulated by 290 nm UV light at reverse bias, as shown in Figure 2a. The device's performance was further conducted under a reverse bias voltage of −1 V. Responsivity, an important evaluation index for photodetectors, can represent the device's sensitivity to a specific wavelength and is defined as $R_\lambda = \frac{I_{ph}}{PS}$, where I_{ph} is the photocurrent of device under a certain wavelength, P is the light power density, and S is the device's area.[10] In addition, the specific detectivity can describe the detection limit of the photodetector and can be defined as $D^* = \frac{R_\lambda}{\sqrt{2qJ_d}}$ as external voltage applied, where q is the electronic charge and J_d is the dark current density.[16] To comprehensively describe the performance of the SMA-based device, responsivities and specific detectivities at various light wavelengths were characterized, as shown in Figure 2b. It is worth noting that the device demonstrated high selectivity toward UV bands and greater detection sensitivity in the solar-blind UV region. Similarly, the specific detectivity curve of the device corresponds to the responsivity curve, exhibiting a greater detection limit in the UVC region. The high selectivity in UV instead of visible light could be attributed to the efficient

separation of excitons via UV excitation. It is suspected that as high-frequency (high-energy) photons excited SMA excess energy with respect to the optical gap would not be totally wasted,[17,18] which can generate thermal charge transfer states, which are delocalized and easily dissociated on heterojunctions;[19] thus, a net gain in charge generation would be produced. A low-frequency (low-energy) light response may require the support of additional energy from the phase separation interfaces to drive them to separate into free carriers.[20]

However, although devices based on single-component SMA presented a spectral window to UV light, the strong crystallinity of SMA introduced a large number of pinholes during the crystallization process (as shown in Figure S1a) that caused radiative loss and leakage current from shunt paths,[16] which adversely impacts the device's photoresponse and dark noise. P3HT presents a smooth film and relatively good optoelectronic performances; thus, it was introduced to weaken the crystallinity during the formation of a layer by SMA (Figure S1d). Polymer organic semiconductor P3HT[21] was introduced into the SMA solution and formed a binary blend of a photosensitive layer. Optoelectronic performances of OPD based on pure P3HT are shown in Figure S2. As shown in Figure 2c, when a small amount of P3HT is doped (13%), the photocurrent of the device is significantly increased by ~10 times. As P3HT is further introduced (33%), the dark current of the device under reverse bias is significantly suppressed by ~10 times, and the photocurrent is further increased by 2 times, where pinholes were successfully suppressed under this condition (Figure S1b,c), resulting in a decrease in the leakage current. Steady-state photoluminescence (PL) measurement confirmed that defects were effectively suppressed by adding 33% P3HT with an ~50% weaker PL intensity than in pure SMA where defects acted as sources of luminescence (Figure S3).

Correspondingly, the responsivity of the device increased by >40 times, the specific detectivity increased by ~200 times, and the optimum device presented a peak responsivity of ~130 mA/W and a specific detectivity of 10^{12} Jones around 290 nm illumination at −1 V (Figure 2d,e). Current−voltage curves of the device with a 67% SMA/33% P3HT photosensitive layer under illumination from UV light to visble light are shown in Figure S4. As the P3HT content continues to increase (70%), the performance of the device begins to decline. Interestingly, shifts of the responsivity curve edges appeared as P3HT was introduced; a specific comparison is given in Figure S5 and Figure 2d, with more refined changes in the ratios of SMA and P3HT, where the responsivity edges were extended from ~400 nm (13%/25% P3HT) to >450 nm (33%) and the broadest responsivity edge appears as 50% P3HT was doped. The responsivity edge comes back to the original state with a further increase in P3HT content (70%). This may be closely related to the degree of phase separation like changing the ratios of SMA and P3HT, which will be discussed below.

The response speed of the photodetector was evaluated by the response time of the device under transient light pulses, as shown in Figure 2f (specific parameters are listed in Table S1). The device depicted a slow speed of 1.25 ms to rise and 57 ms to decay as 13% P3HT was doped. A faster rising speed was achieved with rising time of 0.2 and 0.4 ms as 25% and 33% P3HT, respectively, were doped. As the content of P3HT continued to increase (50% and 70%), the decay speed decreased, with the decay time increasing to 100 and 68 ms,
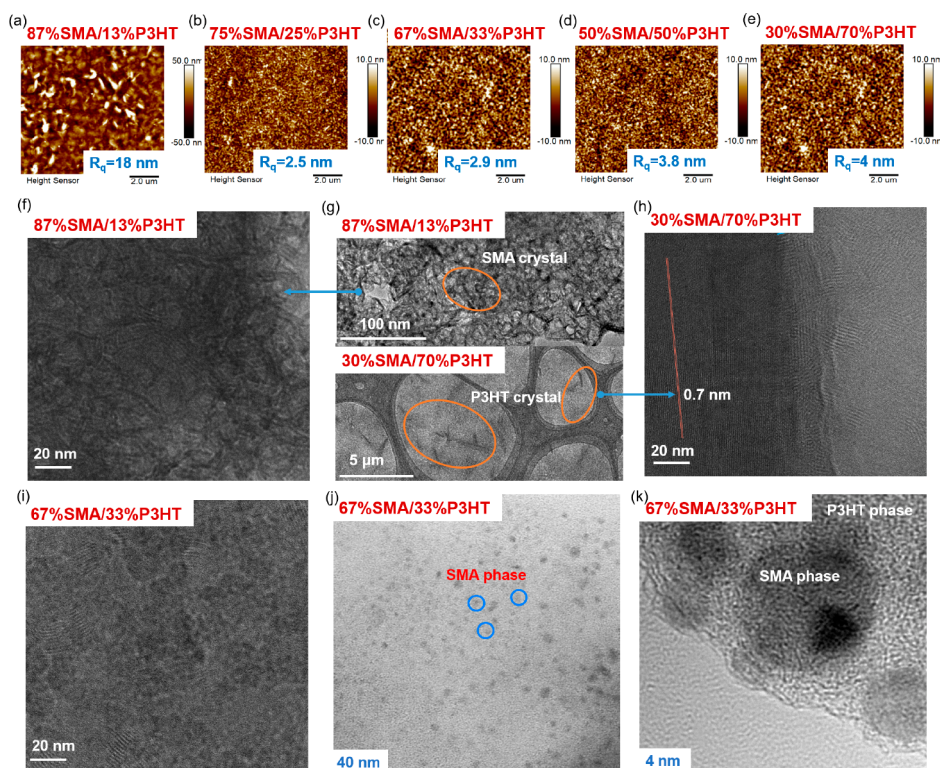
Figure 3. Surface and high-resolution morphologies of the blend with varied P3HT content doping into SMA. Surface morphology by AFM with (a) 87% SMA/13% P3HT, (b) 75% SMA/25% P3HT, (c) 67% SMA/33% P3HT, (d) 50% SMA/50% P3HT, and (e) 30% SMA/70% P3HT blends. High-resolution morphology determined by cryo-transmission electron microscopy with (f) 87% SMA/13% P3HT, (g) 87% SMA/13% P3HT, 30% SMA/70% P3HT, (h) 30% SMA/70% P3HT, and (i) 67% SMA/33% P3HT blends. (j and k) High-resolution morphology by TEM of the 67% SMA/33% P3HT blend.

respectively. Therefore, it is suggested that the doping of a small amount of P3HT (25−33%) can accelerate the separation/transmission of charge carriers under the photoexcited state and the recombination of free charge carriers as the light is switched off. This may closely relate to the regulated phase separation morphology of SMA, which can provide the driving force for facilitating the separation of the electron−hole pairs.

The primary speculation was that introducing second phase P3HT significantly interfered with the crystallization of the SMA film and resulted in differences in the optoelectronic performance of the devices; therefore, it is crucial to further investigate in depth the nanoscale phase separation morphology evolution of organic heterojunctions to understand the separation and transport of charge carriers in photodetectors. First, the surface roughness of the blend layers was characterized by AFM, as shown in Figure 3a−e. The introduction of a small amount of P3HT (to 25% and 33%) interfered with the crystallization of SMA, inducing them to form smaller crystalline domains, which manifested as a decrease in roughness (18 nm in Figure 3a to 2.5 and 2.9 nm in panels b and c, respectively, of Figure 3). Smaller crystalline domains can create more phase separation interfaces, which may increase the possibility of electron−hole separation. With a further increase in P3HT content (to 50% and 70%), due to the poor thermodynamic compatibility between polymer P3HT and SMA, the degree of phase separation continued to increase, manifested as an increase in roughness (3.8 and 4 nm, respectively). With a further increase in P3HT content, the proportion of SMA decreased and the roughness gradually

underwent a transition to a homogeneous system (Figure S6). Actually, an equal SMA:P3HT ratio may correspond to the largest number of phase interfaces, which would statistically provide the maximum driving force for charge separation. Therefore, lower-energy photons could excite the photosensitive layer to generate free carriers (corresponding to the red shift of the response edge like doping with 50% P3HT in Figure 2d). However, evaluating photodetectors requires comprehensive consideration, and it is necessary to seek a balance between responsivity (photocurrent) and specific detectivity (dark current). It has been proven that thermal charge generation at phase separation interfaces may be the primary cause of dark current[13,22] [corresponding to the dark current increase with doping 50% P3HT (Figure S7)]; thus, a SMA-rich blend would acquire the best comprehensive optoelectronic performance in OPD (67% SMA and 33% P3HT).

To observe the crystallization of SMA and P3HT from a nanoscale perspective, we further studied the planar morphology of typical heterostructures directly using TEM. A small amount (13%) of a P3HT-doped blend film exhibited a morphology of tightly packed crystalline grains, where the strong crystallization of small molecules dominated the morphology of the blend film (Figure 3f,g). The strong crystallinity of SMA results in excessive stacking of crystal grains where large defects were induced at the interfaces that would lead to the photocurrent loss caused by radiation recombination and the dark current increase caused by charge injection.[23] When excessive P3HT was doped and became dominant (70%), P3HT phase crystallization occurred (in the
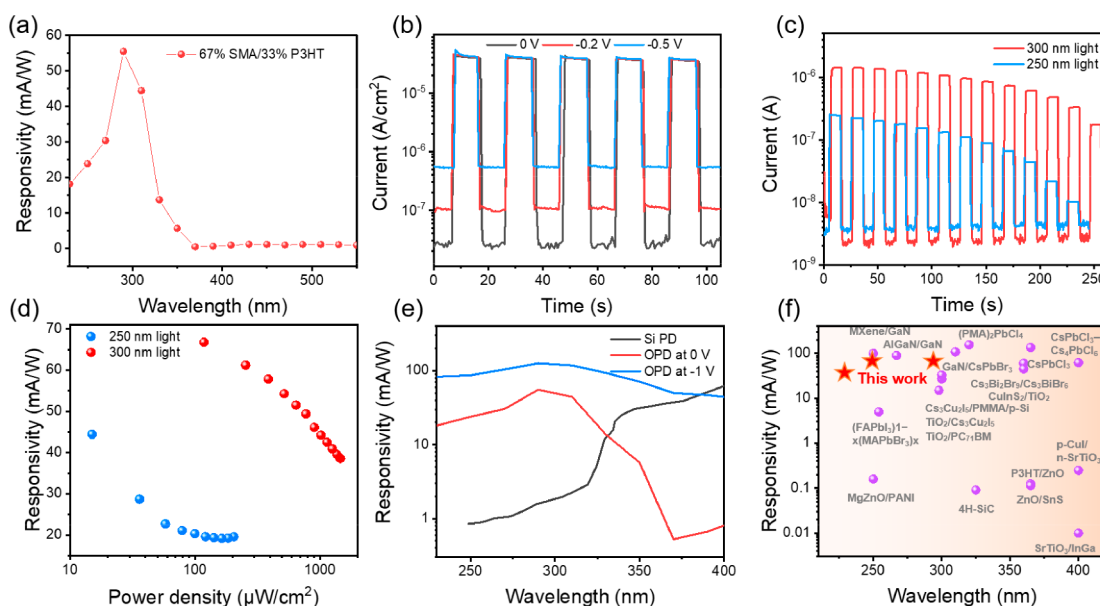
Figure 4. Self-powered performance of the photodetector with a blend of 67% SMA and 33% P3HT. (a) Responsivity of the OPD under different wavelengths of light. (b) Current−time curves of the OPD applied at 0, −0.2, and −0.5 V. (c) Current−time curves and (d) responsivity curves of OPD under illumination with different intensities of light being switched on and off. (e) Responsivities of OPD compared with those of the Si-based photodiode (responsivities of the Si photodiode were obtained from ref 24). (f) Self-powered responsivities of OPD compared with those of reported UV self-powered PD based on other photosensitive materials.[25−42]
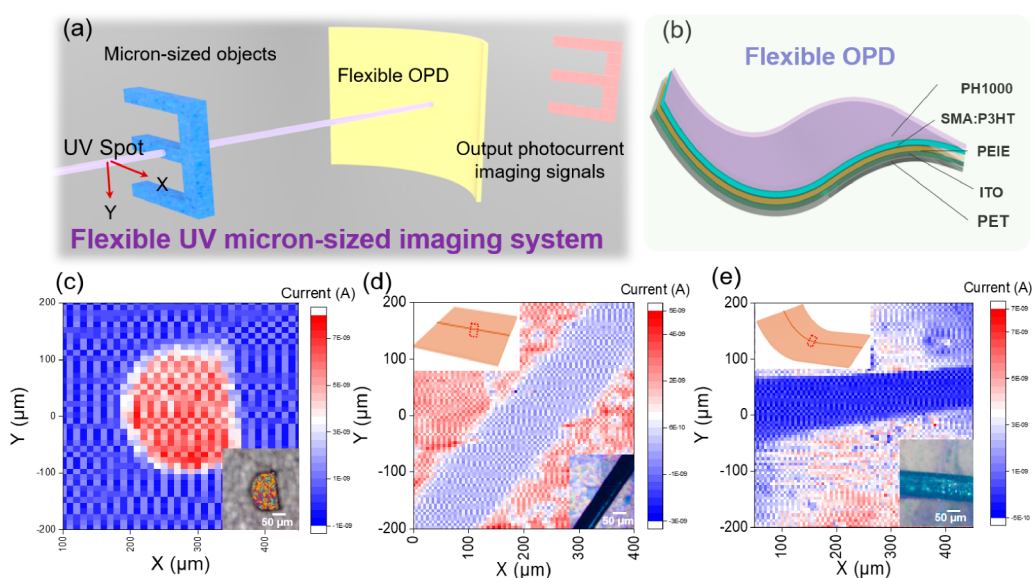
Figure 5. Application in a UV micrometer-sized imaging system. (a) Schematic diagram of a flexible UV micrometer-sized imaging system. (b) Device configuration of flexible OPD. (c) Photocurrent imaging of a letter D based on rigid OPD. Photocurrent images of a hair based on a flexible OPD (d) without and (e) with bending stress applied.

form of long strips, with a length of several micrometers), and a strong crystalline orientation is exhibited, with a $\pi-\pi$ stacking spacing of ~0.7 nm (Figure 3g,h). When a small amount of P3HT (33%) is doped, due to the incompatibility between SMA and polymer P3HT, P3HT plays a "separating" role and suppresses the strong crystallinity of SMA, ultimately making them uniformly dispersed in P3HT (Figure 3i,j) to form appropriate crystalline domains (~20 nm). SMA appears as a dot shape, while P3HT appears as an amorphous shape, as shown in Figure 3k. Defects induced in the grain interface were suppressed, and appropriate phase separation interfaces were

created to provide a driving force for facilitating the separation of electron−hole pairs.

A balanced phase separation morphology achieved with a blend of 67% SMA and 33% P3HT endowed the device with a suppressed dark current and could achieve carrier separation/collection without external bias, operating in photovoltaic mode at 0 V. Figure 4 presents an exhaustive study of the self-powered performance of the optimum device (67% SMA/33% P3HT). The device exhibited excellent UV response selectivity ranging from ~230 to 350 nm, with a half-width of ~50 nm, as shown in Figure 4a. The corresponding external quantum efficiency (EQE) is shown in Figure S8. The current−time

dependence curve shows that as the voltage decreases, the dark current of the device gradually decreases, while the photocurrent of the device is almost unaffected, as shown in Figure 4b. The device can stably output a light:dark ratio of ∼1000 at 0 V. Next, the incident light power densities (corresponding light power densities are listed in Table S2) were changed to study the current−time output of the device, which can still output distinguishable photocurrent−dark current switching signals under weak light signals (100 and 10 μW) (Figure 4c). The device can ultimately output a responsivity of ∼70 mA/W (300 nm) and a deep UV responsivity of 45 mA/W (250 nm) under weak light (Figure 4d). Compared with Si-based photodiodes with a broad spectral response window, this OPD has a competitive advantage in a narrow UV response window, especially at wavelengths below 300 nm, with a responsivity 10−100 times higher than that of the Si photodiode reported recently[24] (Figure 4e). In addition, we summarized the reported responsivity of self-powered UV photodetectors, and high-responsivity devices are mainly dominated by GaN or perovskites combined with other materials, as shown in Figure 4f. The self-powered responsivity of our reported device can be comparable to those of the best-performing devices. Moreover, our device could fill the self-powered device gap with a response below 250 nm.

The reported photocurrent imaging technologies mostly focus on the imaging of large objects (millimeter or centimeter level) due to the constraint of pixel size that relies on the integration of high-density photodetectors.[43] Very little research on imaging of objects of micrometer scale has been reported. The zero-bias operation UV OPD here could simplify the readout electronics and be promising for the construction of a UV micrometer-sized imaging system. Here, a micrometer-sized UV imaging system was realized with a movable UV laser (375 nm), a UV OPD, and a current collector as shown in Figure 5a. Figure S9 shows the uniform current distribution of the device in the dark and light states. The system can scan objects with a size of 100 μm at 400 pixels × 400 pixels, and each pixel has a size of only 5 μm × 5 μm, finally displaying the letter D clearly, as shown in Figure 5c (real-time imaging of the letter D is shown in Figure S10). Second, to demonstrate the unique advantages of organic semiconductors in the field of flexible UV imaging, a flexible device was further prepared with a PET/ITO/PEIE/67% SMA:33% P3HT/PH1000 configuration (Figure 5b), outputting stable on−off currents as the 300 nm UV light was switched on and off (Figure S11). The flexible OPD can achieve clear imaging of hair with a diameter of ∼60 μm (Figure 5d). Moreover, when the flexible OPD and the hair were both bent at a certain angle (30°), the device could still output an imaging pattern of the hair with an inconsistency in the diameter to imply a bending stress was applied on it (Figure 5e).

We started from the chemical structure design to introduce four carbonyl groups in a small-molecule semiconductor to guarantee its absorption intensity in the UV region and finely regulated its crystallization by doping with polymer semiconductor P3HT. Ultimately, we attained an optimized OPD with improved responsivity (improved 10 times) and specific detectivity (improved 100 times), which arose from efficiently suppressed pinholes in SMA with suitable crystallinity and sufficiently separated carriers due to the appropriate phase interfaces (ordered SMA domains). The nanoscale crystallization evolution of the organic heterojunction has been investigated to understand the carrier separation and transport mechanism in photodetectors. It is worth noting that this OPD presents a UV spectral response window with superior self-powered responsivities of 45 mA/W (under 250 nm light) and 70 mA/W (under 300 nm light), outperforming the Si-based photodiode. The zero-bias-operating OPD was applied in a flexible UV imaging system, which can work in the bent state and output micrometer-sized objects. This work reveals the balanced relationship between the morphology of phase domains and the optoelectronic performance of an optoelectronic device, which will provide perspectives on organic semiconductor design and crystallinity control.

■ ASSOCIATED CONTENT

ⓢ Supporting Information

The Supporting Information is available free of charge at https://pubs.acs.org/doi/10.1021/acs.nanolett.3c02511.

Synthesis of SMA, device fabrication, device characterization method, construction of the UV imaging system, CV measurement process, morphology of the blend photosensitive layer, optoelectronic performance of pure P3HT, photoluminescence spectrum intensity of the blend, pure SMA, and pure P3HT, specific optoelectronic parameters of OPD with various SMA:P3HT ratios, responsivity curves under different wavelengths of OPD with different blend ratios, surface morphology of pure P3HT, dark current of OPD with different blend ratios, power densities of 250 and 300 nm light, distribution of the dark current and photocurrent of OPD, current density−time output of the flexible OPD, ^{1}H NMR spectra of SMA, and ^{13}C NMR spectra of SMA (PDF)

■ AUTHOR INFORMATION

Corresponding Author

Xiaosheng Fang − *Department of Materials Science, State Key Laboratory of Molecular Engineering of Polymers, Institute of Optoelectronics, Fudan University, Shanghai 200438, P. R. China;* ⓞ orcid.org/0000-0003-3387-4532; Email: xshfang@fudan.edu.cn

Authors

Tingting Yan − *Department of Materials Science, State Key Laboratory of Molecular Engineering of Polymers, Institute of Optoelectronics, Fudan University, Shanghai 200438, P. R. China*

Jinfeng Ge − *Ningbo Institute of Materials Technology and Engineering, Chinese Academy of Sciences, Ningbo 315201, P. R. China*

Li Su − *Department of Materials Science, State Key Laboratory of Molecular Engineering of Polymers, Institute of Optoelectronics, Fudan University, Shanghai 200438, P. R. China*

Xinya Liu − *Department of Materials Science, State Key Laboratory of Molecular Engineering of Polymers, Institute of Optoelectronics, Fudan University, Shanghai 200438, P. R. China*

Complete contact information is available at:
https://pubs.acs.org/10.1021/acs.nanolett.3c02511

Author Contributions

∥T.Y. and J.G. contributed equally to this work.

REFERENCES

(1) He, J.; Li, C.-Y.; Qi, D.-X.; Cai, Q.; Liu, Y.; Fan, R.-H.; Su, J.; Huo, P.; Xu, T.; Peng, R.; Wang, M. Improving Photoelectric Conversion with Broadband Perovskite Metasurface. *Nano Lett.* **2022**, *22*, 6655−6663.

(2) Chen, Y. H.; Su, L. X.; Jiang, M. M.; Fang, X. S. Switch type PANI/ZnO core-shell microwire heterojunction for UV photodetection. *J. Mater. Sci. Technol.* **2022**, *105*, 259−265.

(3) Su, L.; Yan, T. T.; Liu, X. Y.; Cao, F.; Fang, X. S. A Tunable Polarization Field for Enhanced Performance of Flexible BaTiO$_3$@ TiO$_2$ Nanofiber Photodetector by Suppressing Dark Current to pA Level. *Adv. Funct. Mater.* **2023**, *33*, 2214533.

(4) Xie, C.; Lu, X.-T.; Tong, X.-W.; Zhang, Z.-X.; Liang, F.-X.; Liang, L.; Luo, L.-B.; Wu, Y.-C. Recent Progress in Solar-Blind Deep-Ultraviolet Photodetectors Based on Inorganic Ultrawide Bandgap Semiconductors. *Adv. Funct. Mater.* **2019**, *29*, 1806006.

(5) Li, Z.; Yan, T.; Fang, X. S. Low-dimensional wide-bandgap semiconductors for UV photodetectors. *Nat. Rev. Mater.* **2023**, DOI: 10.1038/s41578-023-00583-9.

(6) Kwon, J.; Takeda, Y.; Shiwaku, R.; Tokito, S.; Cho, K.; Jung, S. Three-dimensional monolithic integration in flexible printed organic transistors. *Nat. Commun.* **2019**, *10*, 54.

(7) Park, K. S.; Baek, J.; Park, Y.; Lee, L.; Hyon, J.; Koo Lee, Y.-E.; Shrestha, N. K.; Kang, Y.; Sung, M. M. Heterogeneous Monolithic Integration of Single-Crystal Organic Materials. *Adv. Mater.* **2017**, *29*, 1603285.

(8) Dong, H.; Zhu, H.; Meng, Q.; Gong, X.; Hu, W. Organic photoresponse materials and devices. *Chem. Soc. Rev.* **2012**, *41*, 1754−1808.

(9) Jiang, T.; Wang, Y.; Zheng, Y.; Wang, L.; He, X.; Li, L.; Deng, Y.; Dong, H.; Tian, H.; Geng, Y.; Xie, L.; Lei, Y.; Ling, H.; Ji, D.; Hu, W. Tetrachromatic vision-inspired neuromorphic sensors with ultraweak ultraviolet detection. *Nat. Commun.* **2023**, *14*, 2281.

(10) García de Arquer, F. P.; Armin, A.; Meredith, P.; Sargent, E. H. Solution-processed semiconductors for next-generation photodetectors. *Nat. Rev. Mater.* **2017**, *2*, 16100.

(11) Yao, Y.; Ou, Q.; Wang, K.; Peng, H.; Fang, F.; Shi, Y.; Wang, Y.; Asperilla, D. I.; Shuai, Z.; Samorì, P. Supramolecular engineering of charge transfer in wide bandgap organic semiconductors with enhanced visible-to-NIR photoresponse. *Nat. Commun.* **2021**, *12*, 3667.

(12) Zhou, Y.; Fei, C.; Uddin, M. A.; Zhao, L.; Ni, Z.; Huang, J. Self-powered perovskite photon-counting detectors. *Nature* **2023**, *616*, 712−718.

(13) Ma, X.; Bin, H.; van Gorkom, B. T.; van der Pol, T. P. A.; Dyson, M. J.; Weijtens, C. H. L.; Fattori, M.; Meskers, S. C. J.; van Breemen, A. J. J. M.; Tordera, D.; Janssen, R. A. J.; Gelinck, G. H. Identification of the Origin of Ultralow Dark Currents in Organic Photodiodes. *Adv. Mater.* **2023**, *35*, 2209598.

(14) Matsuhisa, N.; Niu, S.; O'Neill, S. J. K.; Kang, J.; Ochiai, Y.; Katsumata, T.; Wu, H.-C.; Ashizawa, M.; Wang, G.-J. N.; Zhong, D.; Wang, X.; Gong, X.; Ning, R.; Gong, H.; You, I.; Zheng, Y.; Zhang, Z.; Tok, J. B. H.; Chen, X.; Bao, Z. High-frequency and intrinsically stretchable polymer diodes. *Nature* **2021**, *600*, 246−252.

(15) Zhou, Y.; Fuentes-Hernandez, C.; Shim, J.; Meyer, J.; Giordano, A. J.; Li, H.; Winget, P.; Papadopoulos, T.; Cheun, H.; Kim, J.; Fenoll, M.; Dindar, A.; Haske, W.; Najafabadi, E.; Khan, T. M.; Sojoudi, H.; Barlow, S.; Graham, S.; Brédas, J.-L.; Marder, S. R.; Kahn, A.; Kippelen, B. A Universal Method to Produce Low−Work Function Electrodes for Organic Electronics. *Science* **2012**, *336*, 327−332.

(16) Sandberg, O. J.; Kaiser, C.; Zeiske, S.; Zarrabi, N.; Gielen, S.; Maes, W.; Vandewal, K.; Meredith, P.; Armin, A. Mid-gap trap state-mediated dark current in organic photodiodes. *Nat. Photonics* **2023**, *17*, 368−374.

(17) Grancini, G.; Maiuri, M.; Fazzi, D.; Petrozza, A.; Egelhaaf, H. J.; Brida, D.; Cerullo, G.; Lanzani, G. Hot exciton dissociation in polymer solar cells. *Nat. Mater.* **2013**, *12*, 29−33.

(18) Dimitrov, S. D.; Bakulin, A. A.; Nielsen, C. B.; Schroeder, B. C.; Du, J.; Bronstein, H.; McCulloch, I.; Friend, R. H.; Durrant, J. R. On the Energetic Dependence of Charge Separation in Low-Band-Gap Polymer/Fullerene Blends. *J. Am. Chem. Soc.* **2012**, *134*, 18189−18192.

(19) Bakulin, A. A.; Rao, A.; Pavelyev, V. G.; van Loosdrecht, P. H. M.; Pshenichnikov, M. S.; Niedzialek, D.; Cornil, J.; Beljonne, D.; Friend, R. H. The Role of Driving Energy and Delocalized States for Charge Separation in Organic Semiconductors. *Science* **2012**, *335*, 1340−1344.

(20) Fuentes-Hernandez, C.; Chou, W.-F.; Khan, T. M.; Diniz, L.; Lukens, J.; Larrain, F. A.; Rodriguez-Toro, V. A.; Kippelen, B. Large-area low-noise flexible organic photodiodes for detecting faint visible light. *Science* **2020**, *370*, 698−701.

(21) Nawaz, A.; Meruvia, M. S.; Tarange, D. L.; Gopinathan, S. P.; Kumar, A.; Kumar, A.; Bhunia, H.; Pal, A. J.; Hümmelgen, I. A. High mobility organic field-effect transistors based on defect-free regioregular poly(3-hexylthiophene-2,5-diyl). *Org. Electron.* **2016**, *38*, 89−96.

(22) Go, E.; Jin, H.; Yoon, S.; Park, S.; Park, S. H.; Yu, H.; Son, H. J. Unraveling the Origin of Dark Current in Organic Bulk Heterojunction Photodiodes for Achieving High Near-Infrared Detectivity. *ACS Photonics* **2022**, *9*, 2056−2065.

(23) Zeiske, S.; Sandberg, O. J.; Zarrabi, N.; Li, W.; Meredith, P.; Armin, A. Direct observation of trap-assisted recombination in organic photovoltaic devices. *Nat. Commun.* **2021**, *12*, 3603.

(24) Saha, A.; Kumar, G.; Pradhan, S.; Dash, G.; Viswanatha, R.; Konstantatos, G. Visible-Blind ZnMgO Colloidal Quantum Dot Downconverters Expand Silicon CMOS Sensors Spectral Coverage into Ultraviolet and Enable UV-Band Discrimination. *Adv. Mater.* **2022**, *34*, 2109498.

(25) Biyikli, N.; Aytur, O.; Kimukin, I.; Tut, T.; Ozbay, E. Solar-blind AlGaN-based Schottky photodiodes with low noise and high detectivity. *Appl. Phys. Lett.* **2002**, *81*, 3272−3274.

(26) Cao, F.; Yan, T.; Li, Z.; Wu, L.; Fang, X. S. Dual-Band Perovskite Bulk Heterojunction Self-Powered Photodetector for Encrypted Communication and Imaging. *Adv. Opt. Mater.* **2022**, *10*, 2200786.

(27) Chen, H.; Yu, P.; Zhang, Z.; Teng, F.; Zheng, L.; Hu, K.; Fang, X. S. Ultrasensitive Self-Powered Solar-Blind Deep-Ultraviolet Photodetector Based on All-Solid-State Polyaniline/MgZnO Bilayer. *Small* **2016**, *12*, 5809−5816.

(28) Deng, X.; Li, Z.; Cao, F.; Hong, E.; Fang, X. S. Woven Fibrous Photodetectors for Scalable UV Optical Communication Device. *Adv. Funct. Mater.* **2023**, *33*, 2213334.

(29) Guo, L.; Liu, X.; Cong, R.; Gao, L.; Zhang, K.; Zhao, L.; Wang, X.; Wang, R.-N.; Pan, C.; Yang, Z. Patterned 2D Ferroelectric Perovskite Single-Crystal Arrays for Self-Powered UV Photodetector Boosted by Combining Ferro-Pyro-Phototronic and Piezo-Phototronic Effects. *Nano Lett.* **2022**, *22*, 8241−8249.

(30) Li, M.; Xu, J.; Zhu, K.; Shi, S.; Zhang, Q.; Bu, Y.; Chen, J.; Xu, J.; Zheng, Q.; Su, Y.; Zhang, X.; Li, L. The fabrication of a self-powered CuInS$_2$/TiO$_2$ heterojunction photodetector and its application in visible light communication with ultraviolet light encryption. *J. Mater. Chem. C* **2021**, *9*, 14613−14622.

(31) Li, X.; Zhou, Y.; Huang, F.; Tao, X.; Ouyang, Y.; Mo, X.; Zhao, J. Enhanced self-powered UV photodetection from X chromosome-shaped Cs$_3$Cu$_2$I$_5$ microcrystals. *J. Mater. Chem. C* **2023**, *11*, 5073−5081.

(32) Nguyen, T. M. H.; Lee, S. K.; Kim, S.; Bark, C. W. Practical Demonstration of Deep-Ultraviolet Detection with Wearable and Self-Powered Halide Perovskite-Based Photodetector. *ACS Appl. Mater. Interfaces* **2021**, *13*, 57609−57618.

(33) Ouyang, B.; Zhang, K.; Yang, Y. Self-Powered UV Photo-detector Array Based on P3HT/ZnO Nanowire Array Hetero-junction. *Adv. Mater. Technol.* **2017**, *2*, 1700208.

(34) Ouyang, B.; Zhang, K.; Yang, Y. Photocurrent Polarity Controlled by Light Wavelength in Self-Powered ZnO Nanowires/SnS Photodetector System. *iScience* **2018**, *1*, 16−23.

(35) Song, W.; Chen, J.; Li, Z.; Fang, X. S. Self-Powered MXene/GaN van der Waals Heterojunction Ultraviolet Photodiodes with Superhigh Efficiency and Stable Current Outputs. *Adv. Mater.* **2021**, *33*, 2101059.

(36) Yan, T.; Cai, S.; Hu, Z.; Li, Z.; Fang, X. S. Ultrafast Speed, Dark Current Suppression, and Self-Powered Enhancement in TiO_2-Based Ultraviolet Photodetectors by Organic Layers and Ag Nanowires Regulation. *J. Phys. Chem. Lett.* **2021**, *12*, 9912−9918.

(37) Yang, L.; Tsai, W.-L.; Li, C.-S.; Hsu, B.-W.; Chen, C.-Y.; Wu, C.-I.; Lin, H.-W. High-Quality Conformal Homogeneous All-Vacuum Deposited $CsPbCl_3$ Thin Films and Their UV Photodiode Applications. *ACS Appl. Mater. Interfaces* **2019**, *11*, 47054−47062.

(38) Yang, W.; Zhang, Y.; Zhang, Y.; Deng, W.; Fang, X. S. Transparent Schottky Photodiode Based on AgNi NWs/$SrTiO_3$ Contact with an Ultrafast Photoresponse to Short-Wavelength Blue Light and UV-Shielding Effect. *Adv. Funct. Mater.* **2019**, *29*, 1905923.

(39) Zhang, J.; Jiao, B.; Dai, J.; Wu, D.; Wu, Z.; Bian, L.; Zhao, Y.; Yang, W.; Jiang, M.; Lu, S. Enhance the responsivity and response speed of self-powered ultraviolet photodetector by GaN/$CsPbBr_3$ core-shell nanowire heterojunction and hydrogel. *Nano Energy* **2022**, *100*, 107437.

(40) Zhang, Y.; Liu, H.; Liu, S.; Gong, Q.; Liu, Y.; Tian, D.; Kang, L. Narrowband photoresponse of a self-powered CuI/$SrTiO_3$ purple light detector with an ultraviolet-shielding effect. *J. Mater. Chem. C* **2022**, *11*, 127−133.

(41) Zhang, Y.; Wang, Y.-C.; Wang, L.; Zhu, L.; Wang, Z. L. Highly Sensitive Photoelectric Detection and Imaging Enhanced by the Pyro-Phototronic Effect Based on a Photoinduced Dynamic Schottky Effect in 4H-SiC. *Adv. Mater.* **2022**, *34*, 2204363.

(42) Zhu, W.; Deng, M.; Chen, D.; Zhang, Z.; Chai, W.; Chen, D.; Xi, H.; Zhang, J.; Zhang, C.; Hao, Y. Dual-Phase $CsPbCl_3$−Cs_4PbCl_6 Perovskite Films for Self-Powered, Visible-Blind UV Photodetectors with Fast Response. *ACS Appl. Mater. Interfaces* **2020**, *12*, 32961−32969.

(43) van Breemen, A. J. J. M.; Ollearo, R.; Shanmugam, S.; Peeters, B.; Peters, L. C. J. M.; van de Ketterij, R. L.; Katsouras, I.; Akkerman, H. B.; Frijters, C. H.; Di Giacomo, F.; Veenstra, S.; Andriessen, R.; Janssen, R. A. J.; Meulenkamp, E. A.; Gelinck, G. H. A thin and flexible scanner for fingerprints and documents based on metal halide perovskites. *Nat. Electron.* **2021**, *4*, 818−826.